High-Fidelity Simulations of a Tiltwing Vehicle for Urban Air Mobility

David Garcia Perez*, Patricia Ventura Diaz†, and Seokkwan Yoon‡
NASA Ames Research Center, Moffett Field, California, 94035

NASA is playing an important role in the development of the urban air mobility ecosystem by identifying key research areas and establishing a fleet of conceptual reference vehicles for urban air mobility applications. This paper delves deeper into the study of NASA's six-passenger tiltwing air taxi aerodynamics using high-fidelity computational fluid dynamics simulations. NASA's OVERFLOW flow solver has been loosely-coupled with the rotorcraft comprehensive analysis code CAMRAD II. Dual-time stepping, high-order accurate schemes, and the delayed detached-eddy simulation are employed. The tiltwing configuration is analyzed in airplane and helicopter mode, with flight conditions representative of an air taxi mission. Airloads, wake geometry, and performance are studied to identify the unique flow features of this configuration. NASA's tiltwing vehicle is one of the conceptual designs intended to focus and guide NASA's research activities in support of aircraft development for vertical take-off and landing air taxi operations.

Nomenclature

Greek symbols

Symbol	Description
α	Angle of attack
β_0	Coning angle
β_{1c}	Longitudinal flapping angle
β_{1s}	Lateral flapping angle
η	Propulsive efficiency
Ω	Rotor rotational speed
ϕ	Inflow angle
ψ	Azimuth position
ρ	Fluid density
θ_0	Collective pitch angle

Roman symbols

Symbol	Description
a	Fluid speed of sound
c	Local rotor blade chord length
FM	Figure of merit
h	Flight altitude
M	Mach number
M^2c_c	Sectional chord force coefficient
M^2c_m	Sectional pitching moment coefficient
M^2c_n	Sectional normal force coefficient
P	Rotor power
R	Rotor radius
r	Radial position
T	Rotor thrust
V_∞	Freestream velocity
v_i	Induced velocity
y^+	Non-dimensional viscous wall spacing

Subscripts

Subscript	Description
root	Blade root
tip	Blade tip
total	Lifting line solution from CAMRAD II

I. Introduction

The world is seeing an increasing trend towards urbanization. According to the United Nations, urban areas are projected to house 60 % of the global population by 2030 [1]. Growing population densities along with inefficient transportation systems are leading to an inevitable increase in traffic congestion. This scenario raises the need to rethink mobility in a sustainable way. NASA is working with several private companies and academic partners on this common goal known as urban air mobility (UAM). UAM is envisioned to be a possible solution to accommodate for the need for a

*Research Scientist, Science & Technology Corporation, Computational Physics Branch.
†Research Scientist, Science & Technology Corporation, Computational Physics Branch, Member AIAA.
‡Chief, Computational Physics Branch.

quick, efficient, and reliable transportation system. It will allow passengers or packages to be moved within metropolitan environments. Over the last few years, much research at NASA has focused on the development of urban air taxis.

NASA's Revolutionary Vertical Lift Technology (RVLT) project has been developing tools and datasets to support the design of advanced vertical-lift aircraft [2]. RVLT is establishing a fleet of conceptual air taxi vehicles, with the objective to focus and guide the research activities in support of aircraft development for emerging aviation markets [3–5]. RVLT has also been elaborating various software packages to link individual discipline-based prediction tools into a unified toolchain. RVLT toolchain has been applied to several concept vehicles for the practical design of quieter UAM aircraft: quadrotor, side-by-side, lift-plus-cruise, quiet single-main rotor helicopter, and tiltwing configurations [6].

Among the vehicles proposed across the UAM community, tiltwing is a compelling design. By tilting the wing to the upright position, these aircraft can hover, take-off and land vertically as conventional helicopters. An efficient cruise flight or "airplane-mode" can be achieved tilting the wing back to a horizontal position. Figure 1 shows two examples of tiltwing aircraft configurations: LTV XC-142A, a transport/cargo aircraft developed during the 1960s; and Langley Aerodrome No. 8 (LA-8), which has been developed at NASA Langley Research Center. The LA-8 is a modular design built to gather data on how a tiltwing configuration will perform in the urban environment.

(a) LTV XC-142A tiltwing aircraft, a design featuring 4 rotors.

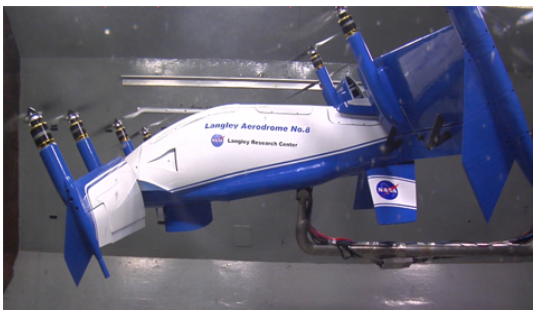

(b) NASA's LA-8 UAM concept, with tandem tiltwing and 8 rotors.

Fig. 1 Examples of aircraft with tiltwing configuration.

NASA's tiltwing vehicle for UAM aims to be representative of industry solutions while considering low-noise objectives. It has been designed to carry a payload of 1200 lb or up to six passengers in two 37.5 nm flights without refueling, with a 20 min reserve [7]. As shown in Fig. 2, it consists of six proprotors positioned on a tilting main wing and two tilting proprotors positioned on the horizontal tail. All proprotors are powered by a turboelectric propulsion system and have collective control. The spin direction —counter-clockwise for rotors on the starboard side and clockwise for rotors on the port side— was chosen for cruise performance, to reduce the strength of the wing tip vortex [8].

(a) Cruise configuration.

(b) Hover and transition configuration.

Fig. 2 Rendering of the tiltwing vehicle design for UAM.

The flow field around the tiltwing aircraft is highly influenced by the aerodynamic interactions between propellers and the wing in the different flight conditions. While hovering, the performance of this configuration might improve in comparison with a tiltrotor aircraft due to the reduced download on the wing, as suggested by Ventura Diaz and

Yoon [9]. A tiltwing configuration is able to perform efficient cruise, eliminating the limitation on forward speed and reducing the noise relative to other UAM reference vehicles.

However, the transition maneuver between hover and forward mode and vice versa still represents an important challenge due to the nonlinear, unsteady, and complex flows involved. In addition, the high angles of attack during transition might cause the wing to stall in some flight conditions. Therefore, an accurate prediction of the flow physics around the aircraft is necessary in order to ensure safe performance and assess the acoustic behavior over the entire flight envelope. High-fidelity computational fluid dynamics (CFD) can predict these complex phenomena, offering an advantage over mid- and low-fidelity tools for this type of flows.

Previous high-fidelity CFD work performed by Ventura Diaz et al. includes simulations of NASA's quiet single-main rotor helicopter [10], NASA's quadrotor isolated rotors [11] and quadrotor complete vehicle [12], NASA's side-by-side air taxi concept [13], and computational analysis of small multi-rotor vehicles [14]. Also, a number of investigations of the interaction between wing and propellers have been conducted in the past using high-fidelity CFD. Ventura Diaz and Yoon [9] carried out an analysis of a box-wing tiltwing aircraft prototype using NASA's high-fidelity OVERFLOW CFD code in hover and cruise. They characterized the aerodynamic interaction of the rotors with the tiltwing, the box-wing and the fuselage in both flight configurations. Tran et al. [15] conducted a study of the Bell XV-15 tiltrotor using OVERFLOW. Their study included different stages of the transition maneuver, from hover mode to cruise condition. Lim [16] studied rotor-wing interactions on a tiltrotor aircraft equipped with the XV-15 rotor in cruise configuration using the Helios framework.

The objectives of the present work are to simulate and analyze NASA's tiltwing UAM concept in airplane and helicopter mode using high-fidelity CFD. Accurate predictions of the blade motions and airloads are retrieved from a coupling between the flow solver and a comprehensive rotorcraft code. The rotor wake geometry, airloads, and performance are analyzed for each case.

II. Numerical Approach

The flow solver used in this study is NASA's OVERFLOW [17] CFD code. OVERFLOW is a finite-difference, structured overset grid, high-order accurate Navier-Stokes flow solver. NASA's Chimera Grid Tools (CGT) [18] software package is used for the overset grid generation of the rotors and the complete vehicle. A common practice for overset grid generation is to write a script in Tcl. Building the script provides control on the entire grid generation process, making it repeatable and allowing for rapid geometry modifications or grid refinement studies. Body-fitted curvilinear near-body (NB) grids are first generated using CGT. The computational domain is then filled with various refinement levels of Cartesian off-body (OB) grids. These grids are automatically generated prior to grid assembly using the domain connectivity framework in OVERFLOW-D mode. The current time-accurate approach consists of an inertial coordinate system where NB curvilinear O-grids for the rotor blades rotate through the fixed OB Cartesian grid system. OVERFLOW is loosely-coupled with the helicopter comprehensive code CAMRAD II [19]. The CFD provides high-fidelity, nonlinear aerodynamic loads that correct the lifting line aerodynamic analysis from CAMRAD II. The comprehensive code performs the structural dynamics and trim calculations and gives the information to OVERFLOW. The loose coupling allows for a modular approach and communication through file input/output. The coupling methodology has been implemented following the approach of Potsdam et al. [20].

The numerical approach and the coupling process are described in more detail in the following subsections.

A. Overset Grid Generation

The overset grid generation process using CGT may be decomposed into four steps: geometry processing, surface grid generation, volume grid generation, and domain connectivity [18].

The geometry is usually obtained from a computer-aided design (CAD) model or a 3D-scanning point cloud. In solid modeling, the boundary representation (BRep) of an object describes its boundaries holding both the topological entities and the geometric components [21]. A pre-processing step generates discrete surface representations from the analytical BRep solid contained in STEP or IGES files. Access to the model topology and entities is accomplished through EGADS (the Engineering Geometry Aircraft Design System) API which is a foundational component of the Engineering Sketch Pad [21]. For each body in the geometry, the `egads2srf` tool generates a surface grid file containing a set of structured surface patches on tessellated untrimmed BRep faces. Figures 3c and 3d show the structured untrimmed patches obtained using EGADS for the tiltwing aircraft. A curve grid file is also created that contains structured curves on tessellated BRep edges. Both files are used as inputs in the overset surface grid generation step.

Once the geometry has been processed as reference curve and surface files, structured surface grids are generated

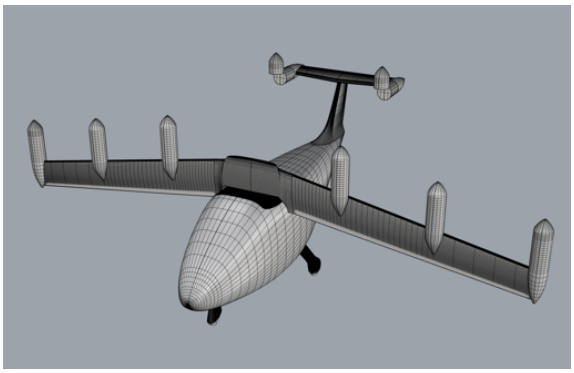

(a) CAD geometry for helicopter mode.

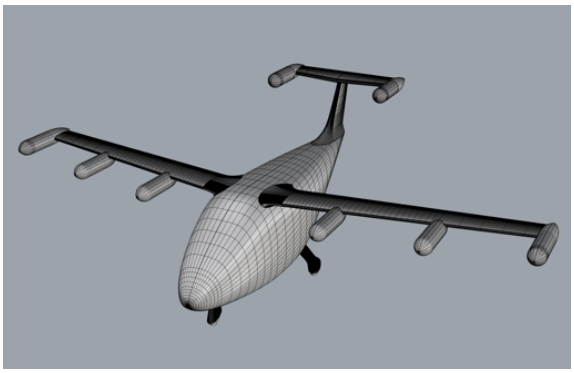

(b) CAD geometry for airplane mode.

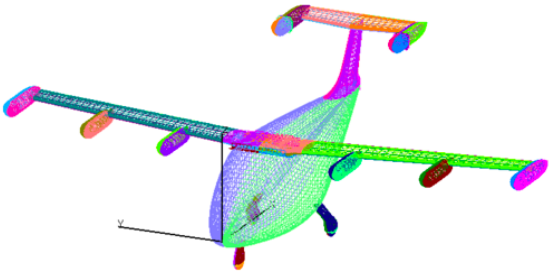

(c) EGADS surface grid for helicopter mode.

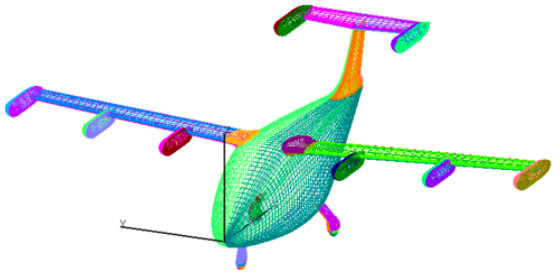

(d) EGADS surface grid for airplane mode.

Fig. 3 The tiltwing vehicle air taxi airframe. Figures 3a and 3b show the CAD geometry for the different flight conditions. Similarly, Figures 3c and 3d show the structured untrimmed patches obtained from the CAD geometry using EGADS. The patches are used as reference surfaces to generate the overset surface grids.

using a combination of algebraic and hyperbolic methods. The generation of surface grids is the step that requires the most manual effort and experience from the user. The CAD geometry for hover —see Fig. 3a— can also be utilized during transition simulations, since it ensures that only one set of grids are generated for the wing and the fuselage, valid for all tilting angles. A one-inch gap is left between both components so that the wing is able to rotate freely relative to the fuselage. In the cruise geometry depicted in Fig. 3b, the gap is filled such that the wing and fuselage are attached together and the sharp corners are smoothed to avoid simulating the flow in the cavity. Figure 4 shows the resulting overset surface grids for the two configurations of the tiltwing UAM concept studied in this work: "airplane mode" in Fig. 4a and "helicopter mode" in Fig. 4b. The complete vehicle consists of the rotors, nacelles, fuselage, wing, tail, and landing gear. The rotor naming convention and spin direction are also indicated in Fig. 4.

If surface grids have sufficient overlap, the volume grids are then created using hyperbolic marching methods which extend the grid out to a fixed distance from the surface. Tight clustering in the normal direction near the wall is maintained to achieve good boundary layer resolution in viscous flow computations. The normal grid spacing of all grids at the walls maintains $y^+ \leq 1$. Mesh orthogonality is maximized to provide better solution accuracy. NB volume grids are extended ensuring that the outer boundaries are outside the boundary layer. The NB grids are contained inside the OB Cartesian grids, which extend to the far-field.

Uniformly spaced off-body Cartesian grids are utilized to resolve important flow features such as the wake region. Many Cartesian grids with successive levels of refinement based on proximity to the body are generated. Each Cartesian grid is twice as coarse as the previous level, and they expand the grid system to the far-field. The uniform spacing of the first OB grid layer, which contains the resolved wake region, is 10 % of the blade tip chord length c_{tip}. Cartesian grids extend to the far-field boundary, which is 25 wing semispans away from the center of the vehicle in all directions.

Table 1 gathers the information used to generate the geometry. The profiles used to build the rotor blades are 10.6 % thick modern airfoils from $r = 0$ to $r = 0.85R$, and 9 % thick modern airfoils from $r = 0.95R$ to the tip $r = R$. The root cutout is $r = 0.2R$. The transition between the two different airfoil sections is smooth —linear interpolation with the radial stations—. The blade has a taper ratio λ of 0.36. The blade grids are shown in detail in Fig. 5. Surface grid

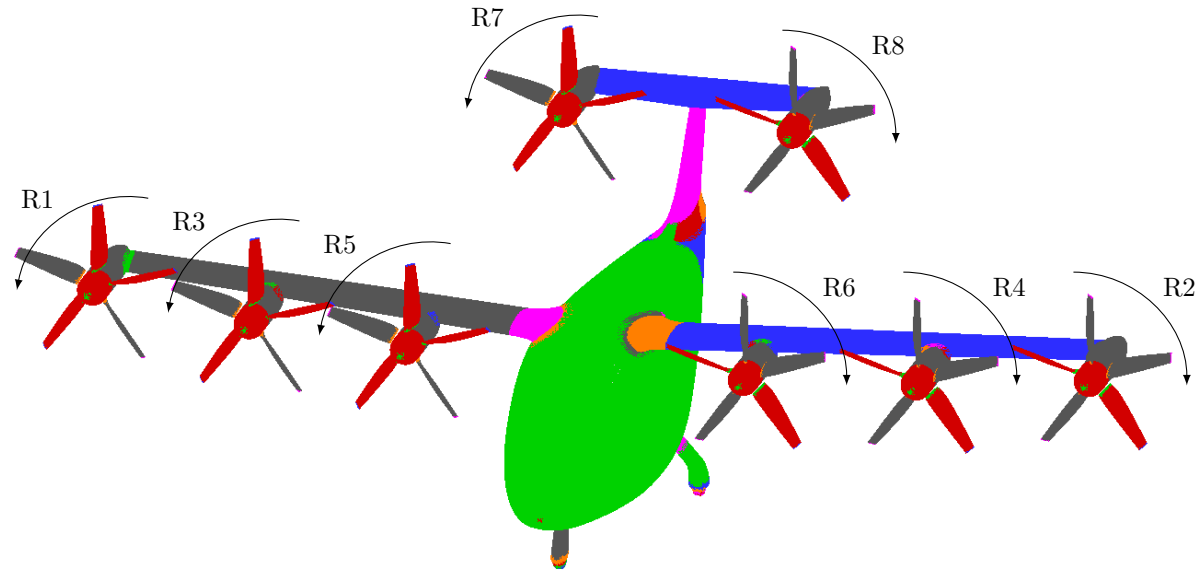

(a) Airplane mode.

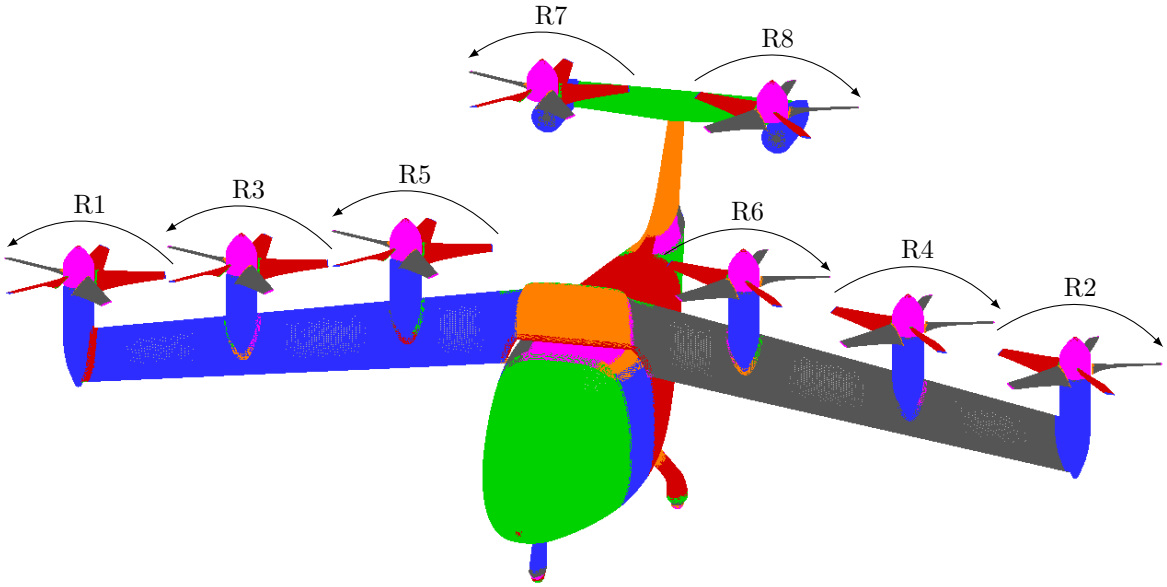

(b) Helicopter mode.

Fig. 4 Tiltwing overset surface grids for the complete vehicle, which includes eight rotors with their corresponding nacelles, fuselage, wing, tail, and landing gear. Figure 4a shows the vehicle with the geometry for cruise condition. Figure 4b shows the geometry designed for the hover case.

Table 1 Summary of parameters related to the tiltwing vehicle.

	Parameter	Value
Rotor	Number of blades/rotor	5
	Radius R	3.666 ft
	Root chord c_{root}	1.252 ft
	Tip chord c_{tip}	0.455 ft
	Thrust-weighted solidity σ	0.2825
	Hover design tip speed V_{tip}	550 ft/s
	Cruise design tip speed V_{tip}	300 ft/s
Main wing	Span b	44.4 ft
	Area A	128 ft^2
	Aspect ratio AR	15.3
Empennage	Horizontal tail span b_{h}	10.2 ft
	Horizontal tail area A_{h}	18.4 ft^2
	Vertical tail span b_{v}	5.28 ft
	Vertical tail area A_{v}	18.4 ft^2
Vehicle	Length l_{f}	28 ft
	Cruise airspeed V_{∞}	145 kt
	Maximum gross weight WMTO	6750 lb

Table 2 Overset grid sizes for the tiltwing vehicle in helicopter and airplane mode.

Configuration	NB grids	NB grid points	NB+OB grid points
Airplane mode	241	158×10^6	420×10^6
Helicopter mode	252	164×10^6	417×10^6

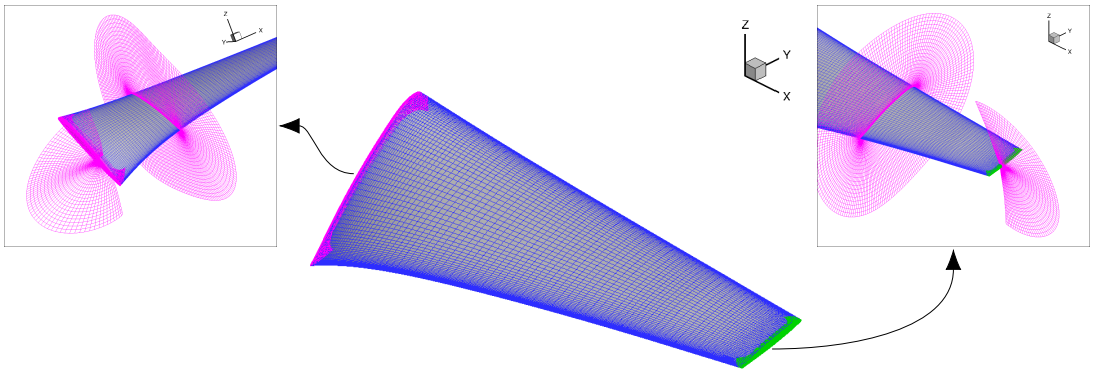

Fig. 5 Blade overset grids for the tiltwing vehicle. O-grids are used for the main blade grid. For the tip and root, cap grids are used. Grid clustering near the leading edge, trailing edge, blade tip and blade root is applied to solve the large pressure gradients near these regions. Slices of volume grids are colored in magenta.

resolution on the rotor blades is clustered in the chordwise direction near the airfoils leading and trailing edges, regions characterized by large pressure gradients. By the same token, the grid resolution is clustered in the spanwise direction near the root and tip.

Domain connectivity issues occur in the overset grid approach as grids arbitrarily overlap with each other, and some points of a grid might lie in the interior of a neighboring component. The domain connectivity step is robust and highly automated when using a trimmed approach. The X-ray hole cutting approach is used in this work. An X-ray object is created for every component of the geometry, i.e., blades, fuselage, landing gear, etc. The user has to supply the list of meshes that each X-ray object is allowed to cut, and an offset distance with which to grow each hole away from the body. Hole cutting is required between components and with the OB grids. This process is performed at each time step within the flow solver, allowing the rotating components to move relative to the fixed components.

Table 2 shows the number of NB grids, and the number of points of NB and OB grids of each configuration analyzed.

B. High-Order Accurate Navier-Stokes Solver

With OVERFLOW, the Navier-Stokes equations can be solved using finite differences with a variety of numerical algorithms and turbulence models. The time-dependent Reynolds-Averaged Navier-Stokes (RANS) equations are solved in strong conservation form:

$$\frac{\partial \boldsymbol{q}}{\partial t} + \frac{\partial (\boldsymbol{F} - \boldsymbol{F}_\mathrm{v})}{\partial x} + \frac{\partial (\boldsymbol{G} - \boldsymbol{G}_\mathrm{v})}{\partial y} + \frac{\partial (\boldsymbol{H} - \boldsymbol{H}_\mathrm{v})}{\partial z} = 0, \tag{1}$$

being $\boldsymbol{q} = [\rho, \rho u, \rho v, \rho w, e]^\intercal$ the vector of conserved variables; $\boldsymbol{F}$, $\boldsymbol{G}$ and $\boldsymbol{H}$ the inviscid flux vectors; and $\boldsymbol{F}_\mathrm{v}$, $\boldsymbol{G}_\mathrm{v}$ and $\boldsymbol{H}_\mathrm{v}$ the viscous flux vectors.

In this study, the diagonal central difference algorithm is used with the 5^{th}-order accurate spatial differencing option with scalar dissipation. The physical time step corresponds to 0.25° rotor rotation, together with up to 50 dual-time sub-iterations for 2.5 to 3.0 orders of magnitude drop in sub-iteration residual. The numerical approach and time step were previously validated for various rotor flows [22–24].

C. Hybrid Turbulence Modeling

The OVERFLOW code currently includes algebraic, one-equation, and two-equation turbulence models, including the choice of hybrid Reynolds-Averaged Navier-Stokes / Large Eddy Simulation (RANS/LES) models that close the RANS equations. In this study, the one equation Spalart-Allmaras [25] turbulence model is used primarily within the boundary layer.

The Detached Eddy Simulation (DES) [25] approach provides a good compromise between accuracy and computational cost. The intent of this model is to combine efficiently the best aspects of RANS and LES methodologies in a single solution. Near-wall regions are treated in RANS mode since turbulent scales can be very small and need to be modeled; and the rest of the flow is treated in LES mode, where the largest turbulent scales are grid-resolved. In this way, DES is a RANS/LES hybrid approach that mitigates the problem of artificially large eddy viscosity. The turbulence length scale d is replaced by $\bar{d}$:

$$\bar{d} = \min(d, C_{\mathrm{DES}} \Delta), \tag{2}$$

which is the minimum of the distance from the wall d and C_{DES} times the local grid spacing Δ.

The DES approach assumes that the wall-parallel grid spacing $\Delta_{||}$ exceeds the thickness of the boundary layer δ so that the RANS model remains active near solid surfaces. If the wall-parallel grid spacing is smaller than the boundary layer thickness, $\Delta_{||} < \delta$ then the DES Reynolds stresses can become under-resolved within the boundary layer; this may lead to non-physical results, including grid-induced separation. Using Delayed Detached Eddy Simulation (DDES) [26], the RANS mode is prolonged and is fully active within the boundary layer. The wall-parallel grid spacing used in this study does not violate the hybrid-LES validity condition; thus, DES and DDES should give similar results. Nevertheless, all computations have been performed using the DDES model for both NB and OB grids.

D. Comprehensive Analysis

Structural dynamics and rotor trim for the coupled calculations are performed using the comprehensive rotorcraft analysis code CAMRAD II [19]. CAMRAD II is a code for the aeromechanics analysis of rotorcraft that incorporates a combination of advanced technologies, including multibody dynamics, nonlinear finite elements, and rotorcraft aerodynamics. The trim task finds the equilibrium solution for a steady-state operating condition, and produces the

solution for performance, loads, and vibration. The aerodynamic model for the rotor blade is based on lifting-line theory, using two-dimensional airfoil characteristics and a vortex wake model. CAMRAD II has undergone extensive correlation with performance and loads measurements on rotorcraft.

E. Loose Coupling OVERFLOW - CAMRAD II

A loose coupling approach between OVERFLOW and CAMRAD II based on a trimmed periodic rotor solution is implemented. The comprehensive code provides the trim solution and blade motions. The high-fidelity CFD calculates the airloads. That is, the CFD airloads replace the comprehensive airloads while using lifting line aerodynamics to trim and computational structural dynamics to account for blade deformations. Figure 6 summarizes the loose coupling approach.

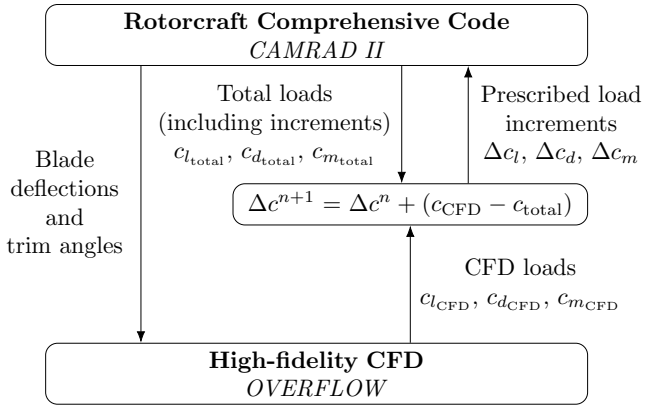

Fig. 6 Flow diagram for CFD/Comprehensive Analysis loose coupling methodology.

The simulation is initialized with a comprehensive analysis resulting in a trimmed rotor solution obtained with lifting line aerodynamics. This analysis creates initial quarter chord motions as a function of the radial position r and the azimuth ψ for the rotor. The motions are given to the CFD. The CFD analysis accounts for the entire flow field, and therefore it only requires the structural motion. The CFD is run with the prescribed motions and angles, for two to three full rotor revolutions for the first coupling step. OVERFLOW outputs the normal force N', pitching moment M', and chord force C' as a function of radius and azimuth. Then, the aerodynamic force and moment coefficient increments Δc that are used in the comprehensive code at the next iteration $n+1$ are calculated. The increments are the difference between the CFD loads and the comprehensive lifting line solution required to trim from the previous step n, plus the load increments from the previous step:

$$\Delta c^{n+1} = \Delta c^n + (c_{\text{CFD}} - c_{\text{total}}). \tag{3}$$

For the initial step, the increments are the difference between CFD and the total loads from the 0^{th} run in CAMRAD II:

$$\Delta c^1 = c_{\text{CFD}} - c_{\text{total}}. \tag{4}$$

The sectional pitching moment $M^2 c_m$, normal force $M^2 c_n$, and chord force $M^2 c_c$ coefficients are defined as:

$$M^2 c_m = \frac{M'}{\frac{1}{2}\rho a^2 c^2}, \tag{5}$$

$$M^2 c_n = \frac{N'}{\frac{1}{2}\rho a^2 c}, \tag{6}$$

$$M^2 c_c = \frac{C'}{\frac{1}{2}\rho a^2 c}. \tag{7}$$

With the new quarter chord motions of the retrimmed rotor, the CFD is rerun. The previous CFD flow solution is used as a restart condition. The coupling is performed every full rotor revolution. Convergence is achieved when

collective and cyclic control angles and the CFD aerodynamic forces do not change between iterations —within a small tolerance. The CFD flow solution is usually converged after 10 to 20 rotor revolutions. The coupling procedure is valid as long as the rotor loads are periodic. This approach still works if there is some aperiodicity in the vortex wake, which is often the case in high-resolution turbulent simulations.

III. Results

NASA's tiltwing air taxi has been simulated in airplane and helicopter mode using the high-fidelity CFD solver OVERFLOW and the rotorcraft comprehensive code CAMRAD II. As discussed above, an iteration involves CAMRAD II providing OVERFLOW with a trimmed flight solution and a set of blade motions. Then, OVERFLOW solves the time-dependent Navier-Stokes equations and provides CAMRAD II with a correction of the airloads. Since the comprehensive code aerodynamics will be replaced by the CFD solution, CAMRAD II uses uniform inflow instead of a free wake model, which allows for a much faster turnaround.

The simulations have been run using NASA's supercomputers Pleiades, Electra, and Aitken located at the NASA Advanced Supercomputing (NAS) Division. In the sections that follow, an analysis of the trim solution, wake geometry, and performance will be presented for each flight condition.

A. Airplane mode

Simulations for cruise are carried out at an altitude of $h = 6000\,\text{ft}$ with a standard atmosphere and a freestream velocity of $V_\infty = 145\,\text{kt}$. The tip speed of the propellers is set to $V_{\text{tip}} = 300\,\text{ft/s}$. The loose coupling is considered converged when the CAMRAD II total blade airloads are equal to the airloads calculated by the CFD, and the trim controls, blade motion, and airloads remain unchanged with the iteration number.

In this flight condition, the rotors act as propulsive devices whereas the wing and horizontal tail should generate the lift required to support the aircraft's weight. By deflecting the elevator, the pilot controls the attitude of the vehicle, changing the angle of attack and lift of the wing. However, control surfaces have not been included for this initial high-fidelity CFD study, and therefore the vehicle's pitching moment will not be zero. Similarly, the vehicle's lift may not match its weight, since the pitch angle Θ is set to zero and not allowed to vary. Even though the trim is not complete, these results still provide valuable preliminary insights into the interactional aerodynamics, development of the wake, and rotor performance.

1. Trim solution

By the end of the simulation, the rotors have rotated 30 revolutions. Table 3 gathers the time average of thrust and torque coefficients for each rotor over the last rotor revolution. The results are divided into three columns: "OVERFLOW", which shows the values calculated by the CFD solution; "CAMRAD II", which presents the coefficients obtained by the comprehensive code using the CFD airloads correction from the previous coupling step; and "Percentage

Table 3 Converged thrust and torque coefficients for the rotors in airplane mode, as seen in OVERFLOW and CAMRAD II.

	OVERFLOW		CAMRAD II		Percentage error	
	$C_T \times 10^3$ [1]	$C_Q \times 10^3$ [1]	$C_T \times 10^3$ [1]	$C_Q \times 10^3$ [1]	Thrust [%]	Torque [%]
Rotor 1	9.127	10.494	9.003	10.521	1.38	−0.26
Rotor 2	9.126	−10.493	9.005	−10.519	1.34	−0.26
Rotor 3	9.031	10.392	8.931	10.437	1.12	−0.44
Rotor 4	9.029	−10.389	8.932	−10.443	1.08	−0.51
Rotor 5	7.017	8.614	6.863	8.642	2.25	−0.33
Rotor 6	7.015	−8.612	6.864	−8.642	2.21	−0.35
Rotor 7	10.549	11.519	10.385	11.533	1.58	−0.12
Rotor 8	10.490	−11.474	10.355	−11.512	1.31	−0.33

error", which shows the relative error of the OVERFLOW airloads with respect to the CAMRAD II solution, expressed as a percentage. The values calculated with the two methods show excellent agreement, especially in the torque coefficients, with the largest discrepancy being 0.51 % of the comprehensive code solution. For the thrust coefficients, this number rises to 2.25 %. Relative errors of less than 3 % in airloads are acceptable to deem the coupled approach converged.

Symmetric rotors produce the same amount of thrust and apply opposite torques to the airframe, which prevent it from yawing and rolling. The presence of the airframe introduces variations in rotor performance with respect to the isolated case. These changes, due to mutual aerodynamic interactions, depend on the rotor placement. In particular, rotors positioned inboard on the wing (5–6) experiment a reduction in total thrust produced. Following the spanwise direction, the fuselage's influence is reduced thus the thrust increases for the middle and outboard rotors. The thrust is slightly higher for the latter presumably due to the influence of the wing tip vortex. The highest thrust coefficients are found for the rotors located on the tail (7–8). Similar trends are observed in the torque coefficient C_Q. These results will translate to differences in performance, as will be shown later.

The time history of the thrust and torque coefficients is plotted in Fig. 7. The results of the CFD solution and the comprehensive code are presented as one-revolution azimuthal averages. Initially, CAMRAD II predicts the same thrust and torque for all rotors, contrarily to OVERFLOW. Subsequent iterations tend to equalize the results based on the delta airloads interfaced between both. Good convergence is achieved after 20 coupling cycles. Consistent with the information presented in Table 3, thrust and torque decrease from the initial CAMRAD II calculations for the inboard rotors (5–6) and increase for the tail rotors (7–8). Only minor variations are observed for rotors 1–2 and 3–4.

Next, the convergence history of the coning angle β_0, longitudinal flapping β_{1c}, lateral flapping β_{1s}, and collective pitch θ_0 angles for each rotor is presented in Fig. 8. Again, an initial CAMRAD II run with uniform inflow finds the same trim solution for all rotors. The variation of the coning and tip-path-plane tilt angles is similar for pairs of symmetric rotors and very small in absolute terms. The coning angle β_0 sees a decrease from the initial trim and reaches a plateau after 20 coupling cycles. It is determined by the equilibrium of inertial and aerodynamic forces acting on the blades. Since the effect of the centrifugal forces is the same for all rotors, a higher thrust produced by the tail rotors (7–8) yields higher coning angles. Conversely, inboard rotors (5–6) produce the least amount of thrust and thus trim to the lowest values, in accordance with the results shown in Table 3. A converged solution for the flapping angles β_{1c} and β_{1c} is achieved faster, after 5 coupling steps. Flapping dynamics changes the angle of attack of the blade sections α with the azimuth ψ thereby some degree of asymmetry is expected in the aerodynamic loads. Finally, the collective pitch angle θ_0 evolves in the same fashion for all rotors, steadily increasing until a converged solution after 20 coupling cycles.

In order to further investigate the differences between the blade loading of the rotors, contour maps of the sectional normal force coefficient $M^2 c_n$ and chord force coefficient $M^2 c_c$ are shown in Figs. 9 and 10, respectively. The coefficients are non-dimensionalized by the speed of sound. Rotor maps are plotted on the disk planes and seen from an upstream position. The azimuth angle ψ is measured from the top, positive in the direction of rotation, and divides the rotor area into four quadrants of 90° each. Note that quadrant locations are reversed when comparing port and starboard side rotors to follow the rotor rotational direction.

Isolated rotors in axial flight would normally be loaded axisymmetrically, with forces and moments increasing towards the tip due to a higher dynamic pressure. With the complete vehicle, however, the flow field is not only influenced by each component but also by their mutual interactions. For example, rotor-airframe beneficial interferences manifest in the normal force coefficients for inboard rotors (5–6) —see Fig. 9— as peaks of lift towards the tip in the third quadrant, when the blade is moving upwards next to the fuselage. A small negative-thrust area is also observed primarily in the fourth quadrant in the root region. These effects decrease with the distance from the fuselage, thereby yielding almost axisymmetric contours for the middle (3–4) and outboard main wing rotors (1–2). Rotor-rotor interactions are the major source of dissymmetry for tail rotors (7–8) as they spin in opposite directions close to each other. In addition, these rotors also interact with the wake of the front rotors. Peaks of lift are encountered in the third and fourth quadrants near the tips whereas a region of negative thrust is observed near the root in the first and second quadrants.

Negative-thrust areas appear as the result of the rotational speed, axial flow through the rotor, and blade flapping which, combined, reduce the angle of attack of the blade sections and produce negative thrust. In a first approximation, according to the blade element theory —see Fig. 11—, the aerodynamic angle of attack α of a cross-section of the blade is the difference between the pitch angle θ and the inflow angle ϕ:

$$\alpha = \theta - \phi = \theta - \arctan \frac{V_\infty + v_i}{\Omega r}. \tag{8}$$

Since the flapping angles are very small, their effect has been neglected for this preliminary analysis. The pitch angle is

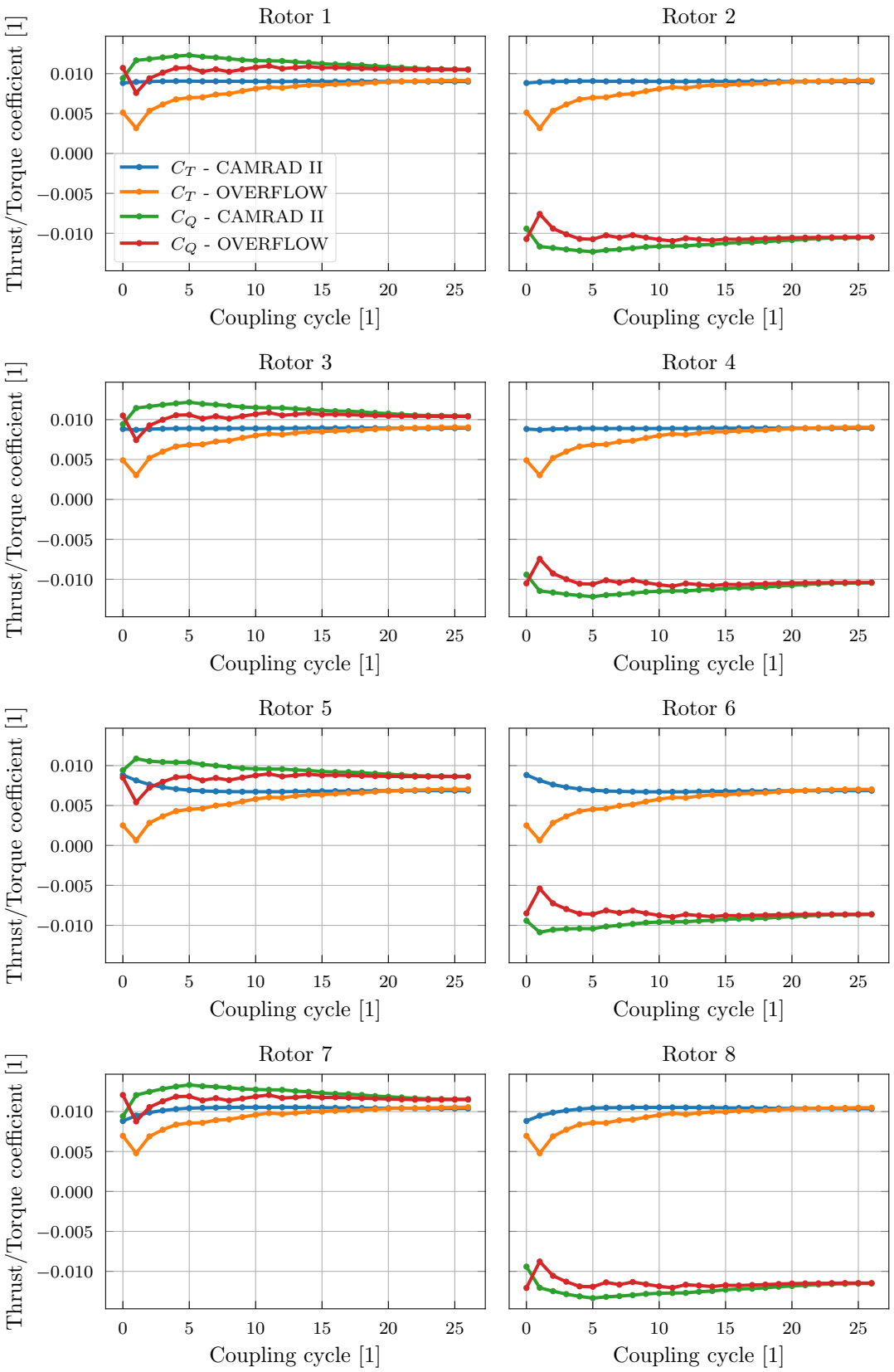

Fig. 7 Convergence history of thrust and torque coefficients in airplane mode.

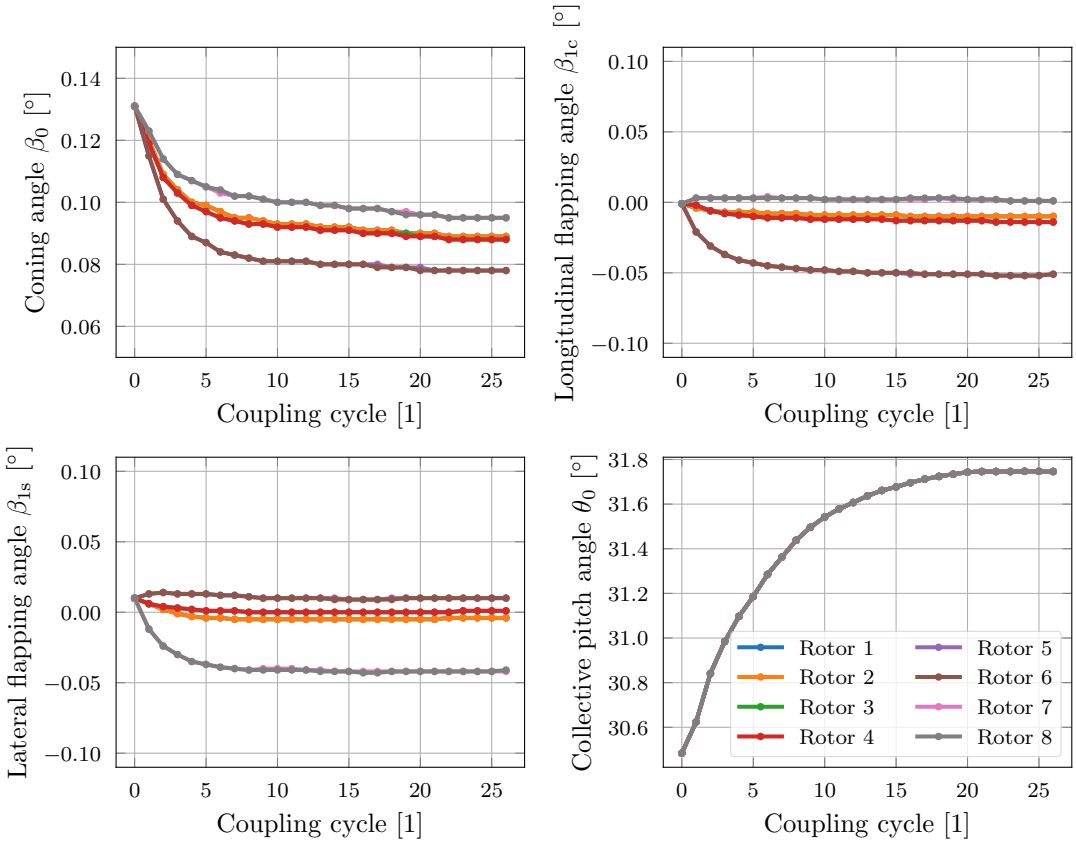

Fig. 8 Convergence history of the rotor trim angles in airplane mode.

the sum of the collective pitch —note that the cyclic pitch angles are zero— and geometric twist. The inflow angle is determined by the components of the local velocity vector: an in-plane velocity Ωr due to the rotation of the blades, and the normal velocity given by the freestream velocity and the induced velocity $V_\infty + v_\mathrm{i}$. Across the entire rotor disk, the axial flow dominated by the freestream component produces a large inflow angle. This angle is further increased near the root where the in-plane velocity is small for radial positions close to the axis of rotation. As a consequence, these cross-sections of the blade see a negative angle of attack, and areas of no-thrust appear. Their location and extension will also depend on other factors such as the disturbances introduced to the inflow of the propellers by the airframe. To mitigate the effect of large inflow angles, the blades are highly twisted near the root and are trimmed to a high collective pitch compared to the hovering case, as seen in Fig. 8.

Similar tendencies are found for the sectional chord force coefficients plotted in Fig. 10. The degree of dissymmetry increases with the proximity to the fuselage. Rotors 1–2 and 3–4 operate close to blade vortices shed by rotors 3–4 and 5–6, respectively, which shows up as discontinuities when the blades transition from the third to the fourth quadrant. In this scenario, an ascending blade encounters descending tip vortices.

To conclude the analysis of the trim solution, the contributions of each component to the vertical force F_z are presented in Fig. 12. The results are averaged over a rotor revolution, with one revolution equivalent to 1440 steps. Wing and tail rotors are grouped for the sake of simplicity. A horizontal dashed line marks the vehicle's gross weight. The gray solid line represents the evolution of the total aerodynamic vertical force acting on the vehicle. These lines should be coincident to maintain a stationary level flight. As was discussed before, without control surfaces and changes in the aircraft's attitude, the wing and the horizontal tail are unable to produce enough lift to support the weight.

In conventional fixed-wing aircraft, it is common for the tail to generate a down-force for longitudinal stability, as it counteracts the turning moment produced by the wing about the center of gravity (CG). In this case, the tail generates a "positive" lift due to the location of the CG between the mean aerodynamic centers of the wing and tail. Future simulations of a transition corridor will include a geometry with control surfaces.

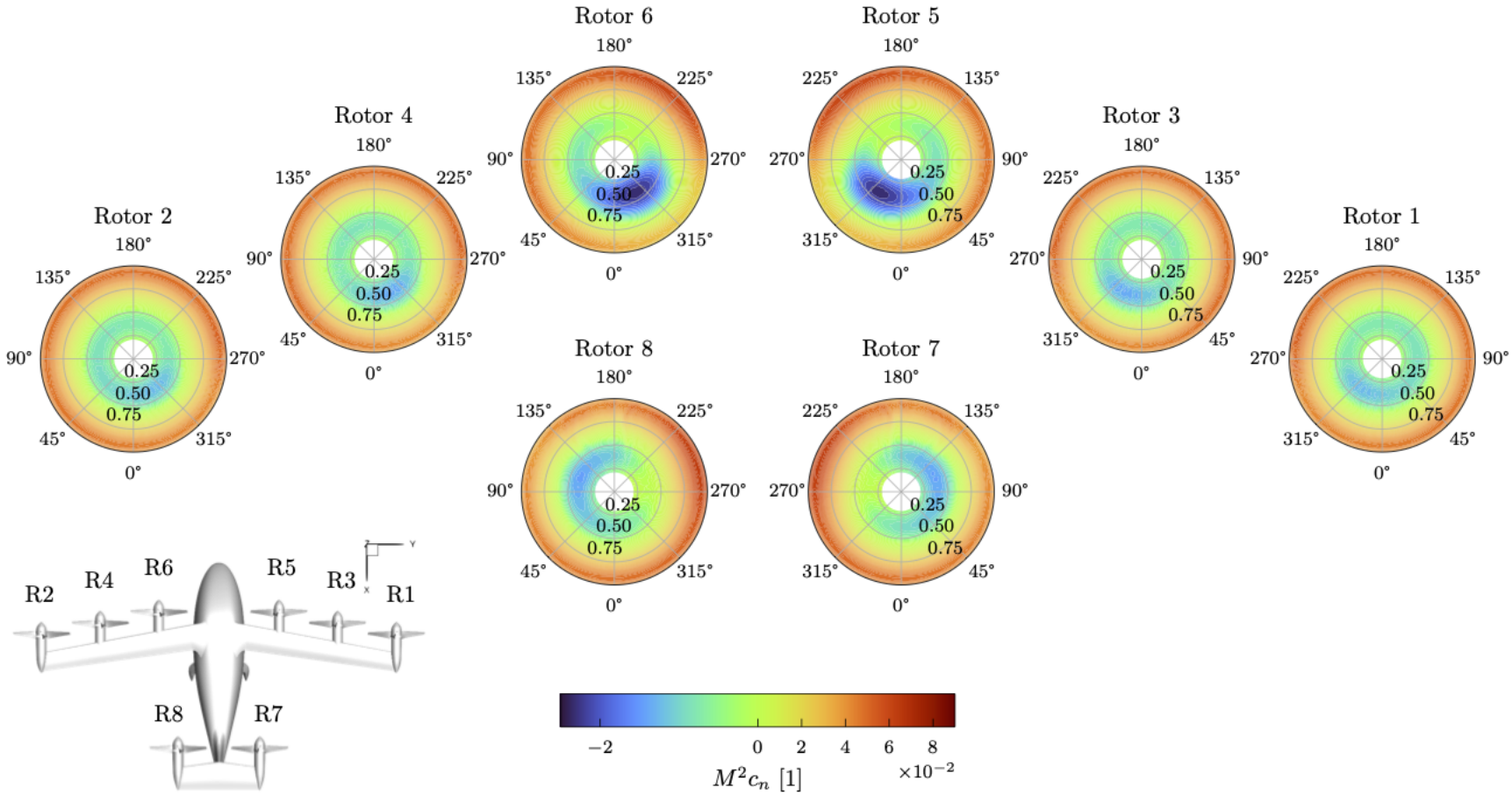

Fig. 9 Sectional normal force coefficient M^2c_n in airplane mode.

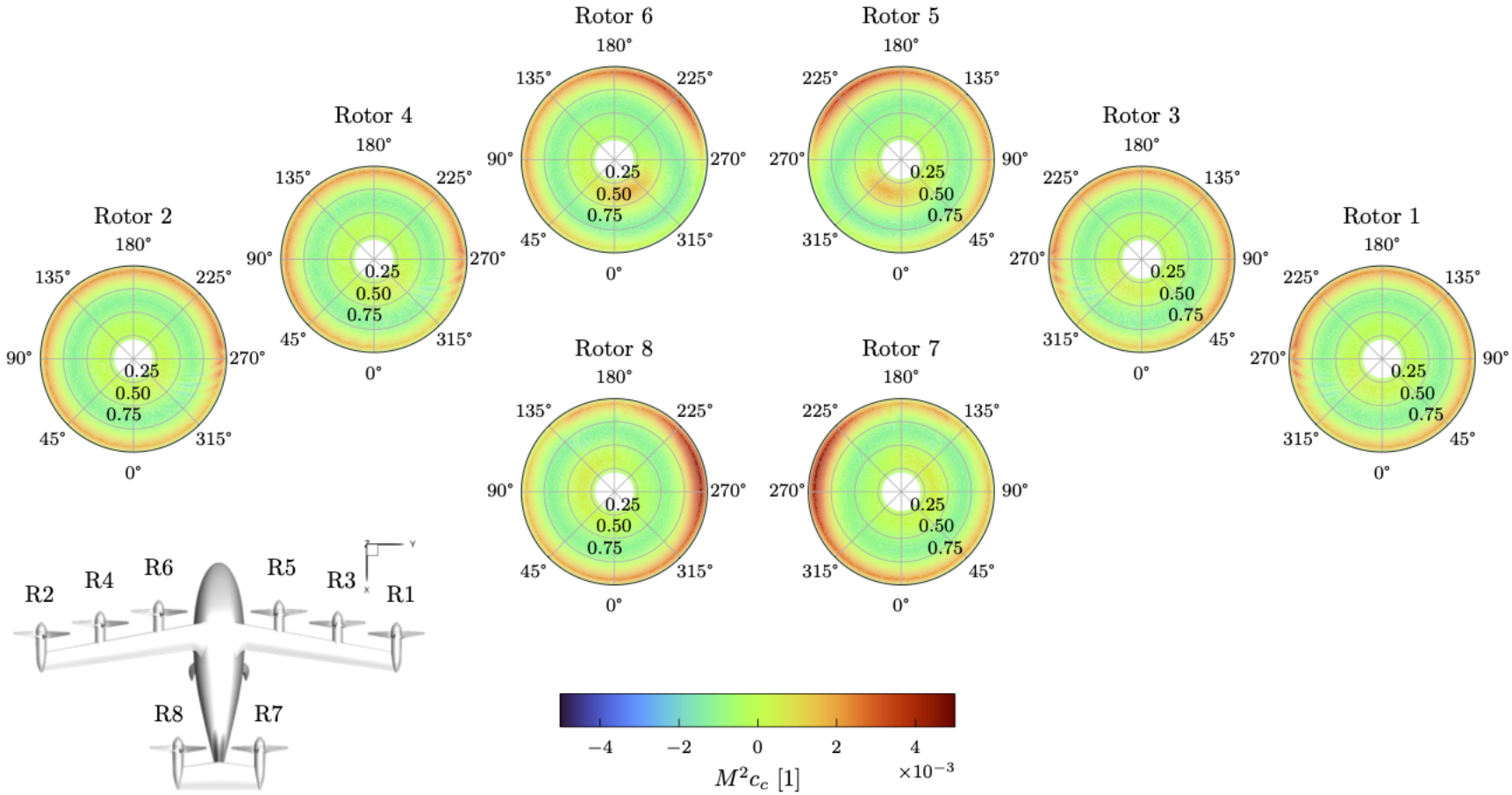

Fig. 10 Sectional chord force coefficient M^2c_c in airplane mode.

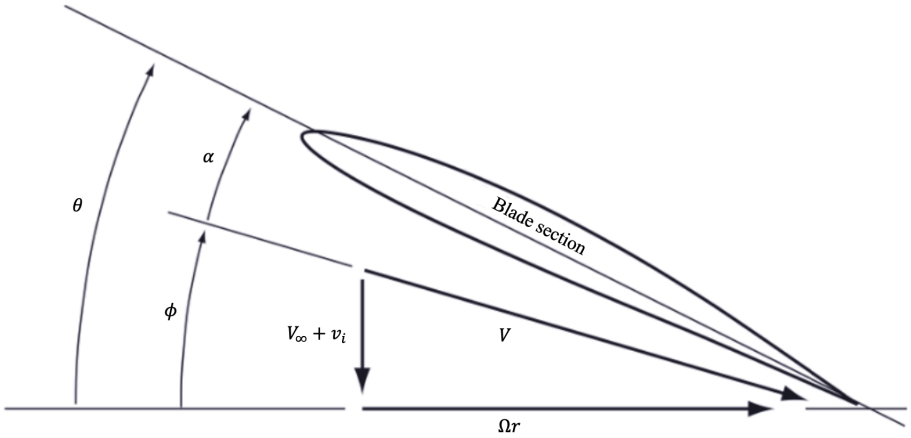

Fig. 11 Triangle of velocities relative to a generic blade section.

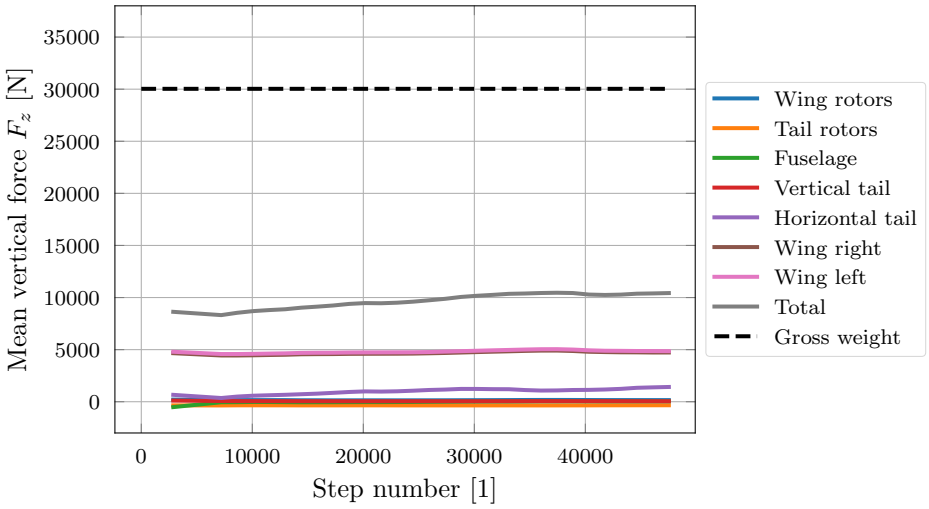

Fig. 12 Equilibrium of the mean vertical force as a function of the time step in airplane mode.

2. Wake geometry

Vortices are visualized through the representation of iso-surfaces of Q-criterion shaded by vorticity magnitude. Figure 13 shows an oblique, top, and front view of the vortex wake. Tip vortices trailed from each blade trace out helical trajectories downstream of the rotors, as a result of the combination of the axial flow passing through the rotor disks and the rotational motion of the blades. A similar root-vortex structure can be also seen followed by its disintegration. The axial freestream velocity causes rapid convection of the vortex wake and reduces the interaction with neighboring blades, resulting in a weak vortex breakdown. Even though it means having stronger rotor-rotor interactions, the rotors are positioned close to each other so that the wing is blown uniformly across the span. This aims to avoid flow separation on the wing during transition maneuvers from helicopter to airplane mode and viceversa. Rotor-wing interactions are influenced by their proximity and will be studied in a future paper. Rotor-wake interactions are observed clearly in Fig. 13c, as the wakes of inboard wing rotors (5–6) collide with tail rotors (7–8) in the azimuthal range $90° < \psi < 180°$, and are swept towards the fuselage. In addition, blade tip vortices strike on the wing and horizontal tail with a frequency of 5 strikes per rotor revolution, and vortex filaments are periodically cut. This interaction may lead to unsteady loading and explain the fluctuations of vorticity magnitude seen on the tail surface. Figure 13b shows how tip vortices from adjacent rotors intertwine with each other. The spin direction of the rotors opposes that of the wing and tail tip vortices in order to reduce their strength and improve cruise performance. Separated flow from the nacelles, fuselage, and landing gear is also observed.

3. Performance

The performance of the cruise operation is measured in terms of propulsive efficiency η. This parameter relates the propulsive power to the input power:

$$\eta = \frac{TV_\infty}{P}, \tag{9}$$

with T being the rotor thrust, V_∞ the rotor velocity with respect to the air, and P the input power.

The propulsive efficiencies for each rotor were obtained from the coupled OVERFLOW/CAMRAD II approach. In addition, a CAMRAD II free wake analysis was also performed for comparison purposes. The implementation of the free wake model in CAMRAD II has been validated extensively over the years and provides a more accurate solution than simpler models like uniform inflow. With respect to the high-fidelity CFD, it has the advantage of a faster turnaround time, since the simulations can be run on a single processor and finish in less than an hour. The predicted propulsive efficiencies show good agreement with those obtained from the high-fidelity CFD, as observed in Table 4. With the exception of the tail rotors (7–8), the propulsive efficiencies predicted by the free wake analysis are higher. Percentage errors with respect to the CFD solution usually range from 2–3 %. Larger discrepancies, up to 9 %, are found for inboard rotors (5–6). The results here obtained are left as a reference for future validation with experimental data.

Table 4 Rotor performance in airplane mode measured by the propulsive efficiency. The results are obtained from the coupled OVERFLOW/CAMRAD II approach and using CAMRAD II free wake analysis.

	Propulsive efficiency η	
	OVERFLOW/CAMRAD II	CAMRAD II free wake
Rotor 1	0.6978	0.7149
Rotor 2	0.6982	0.7149
Rotor 3	0.6973	0.7113
Rotor 4	0.6971	0.7113
Rotor 5	0.6460	0.7086
Rotor 6	0.6461	0.7086
Rotor 7	0.7385	0.7138
Rotor 8	0.7377	0.7138

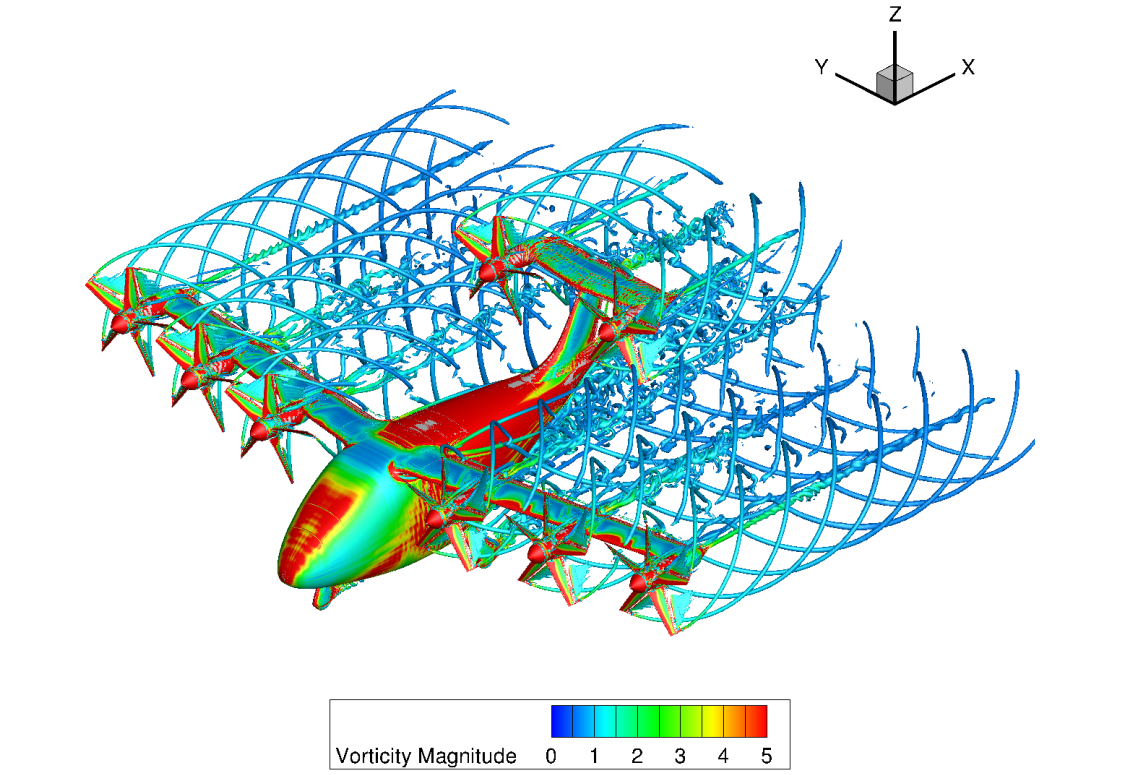

(a) Oblique view.

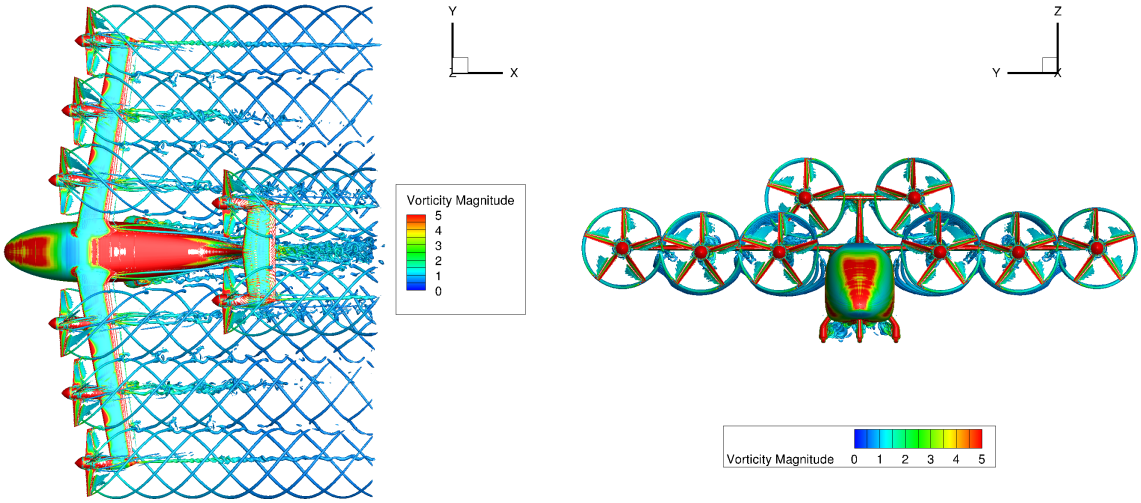

(b) Top view.

(c) Front view.

Fig. 13 Visualization of the wake geometry in airplane mode through the representation of iso-surfaces of Q-criterion colored by vorticity magnitude.

B. Helicopter mode

Simulations in hover are carried out at an altitude of $h = 6000\,\text{ft}$ with a standard atmosphere, and the tip speed of the propellers set to $V_{\text{tip}} = 550\,\text{ft/s}$.

In helicopter mode, the thrust generated by the rotors supports the aircraft's weight. The trim of the vehicle is achieved only through collective control and thus the control surfaces are less relevant. As far as the wing and rotors are concerned, this flight condition is a particular case of axial flow with zero axial velocity. As a consequence, blade tip vortices will remain below the rotor planes for appreciable time. Interactions among vortices are stronger, which makes the CFD solution harder to converge. This section presents a similar analysis to that conducted for airplane mode.

1. Trim solution

The rotors have rotated 35 revolutions at the end of the simulation. Table 5 compares the time average of the thrust and torque coefficients over the last rotor revolution obtained from OVERFLOW and CAMRAD II. On convergence, the CFD airloads replace the lifting line aerodynamics of the comprehensive code. The maximum difference between the last two coupling steps —note that CAMRAD II uses the correction of the second-to-last step— amounts to 0.28 % of the CAMRAD II value for the thrust coefficient C_{T}, and 1.87 % for the torque coefficient C_{Q}. Torque percentage differences are higher in helicopter mode whereas thrust percentage differences are higher in airplane mode.

All rotors produce a similar share of thrust, which is slightly reduced for the rotors closer to the fuselage. Aerodynamic interactions with the airframe yield fewer differences between rotors than those found in airplane mode. The symmetry between the port and starboard side rotors cancels out their contribution to yawing and rolling moments about the center of gravity of the vehicle. Note that these loads will still be transferred to the rotor support structure as bending and twisting moments.

Figure 14 illustrates the evolution of the azimuthal averages of thrust and torque coefficients with the coupling cycle. The curves plotted show a similar convergence history for all rotors. The initial revolutions in OVERFLOW are used to establish the flow solution. For the thrust coefficient, it is in these initial revolutions that the largest discrepancies with the comprehensive code are observed. After about 25 coupling cycles, the results are almost equalized, with only small variations between the subsequent iterations. The torque coefficients already match well after 10 coupling steps.

Figure 15 shows the time history of the coning angle β_0, longitudinal flapping $\beta_{1\text{c}}$, lateral flapping $\beta_{1\text{s}}$, and collective pitch θ_0 angles. The evolution of the trim angles is similar for opposite rotors. The coning angle β_0 is almost converged after 20 iterations and remains unchanged during the last three. The results are consistent with the differences in rotor thrust seen in Table 5. Since all rotors are subjected to the same inertial effects, the trim solution for β_0 is determined by the aerodynamic forces. The tip-path-plane tilt angles initially trim to zero when CAMRAD II uses a uniform inflow model. An isolated rotor operating in hover has a constant flap angle with the azimuth since the disk is loaded symmetrically. In this case, aerodynamic interactions break the azimuthal symmetry, and thus $\beta_{1\text{c}}$ and $\beta_{1\text{s}}$ trim to non-zero values. A sudden peak observed after 21 coupling steps for some rotors is due to the restart of the simulation. The evolution of the collective pith angle θ_0 is similar for wing and tail rotors, with the latter trimming to slightly lower values.

Table 5 Converged thrust and torque coefficients for the rotors in helicopter mode, as seen in OVERFLOW and CAMRAD II.

	OVERFLOW		CAMRAD II		Percentage error	
	$C_T \times 10^2$ [1]	$C_Q \times 10^3$ [1]	$C_T \times 10^2$ [1]	$C_Q \times 10^3$ [1]	Thrust [%]	Torque [%]
Rotor 1	3.404	6.638	3.402	6.730	0.07	−1.36
Rotor 2	3.407	−6.632	3.405	−6.725	0.06	−1.38
Rotor 3	3.316	6.420	3.324	6.539	−0.26	−1.82
Rotor 4	3.315	−6.418	3.319	−6.525	−0.11	−1.64
Rotor 5	3.264	6.328	3.262	6.435	0.07	−1.66
Rotor 6	3.262	−6.321	3.265	−6.441	−0.08	−1.87
Rotor 7	3.303	6.298	3.312	6.407	−0.28	−1.70
Rotor 8	3.305	−6.301	3.312	−6.412	−0.21	−1.74

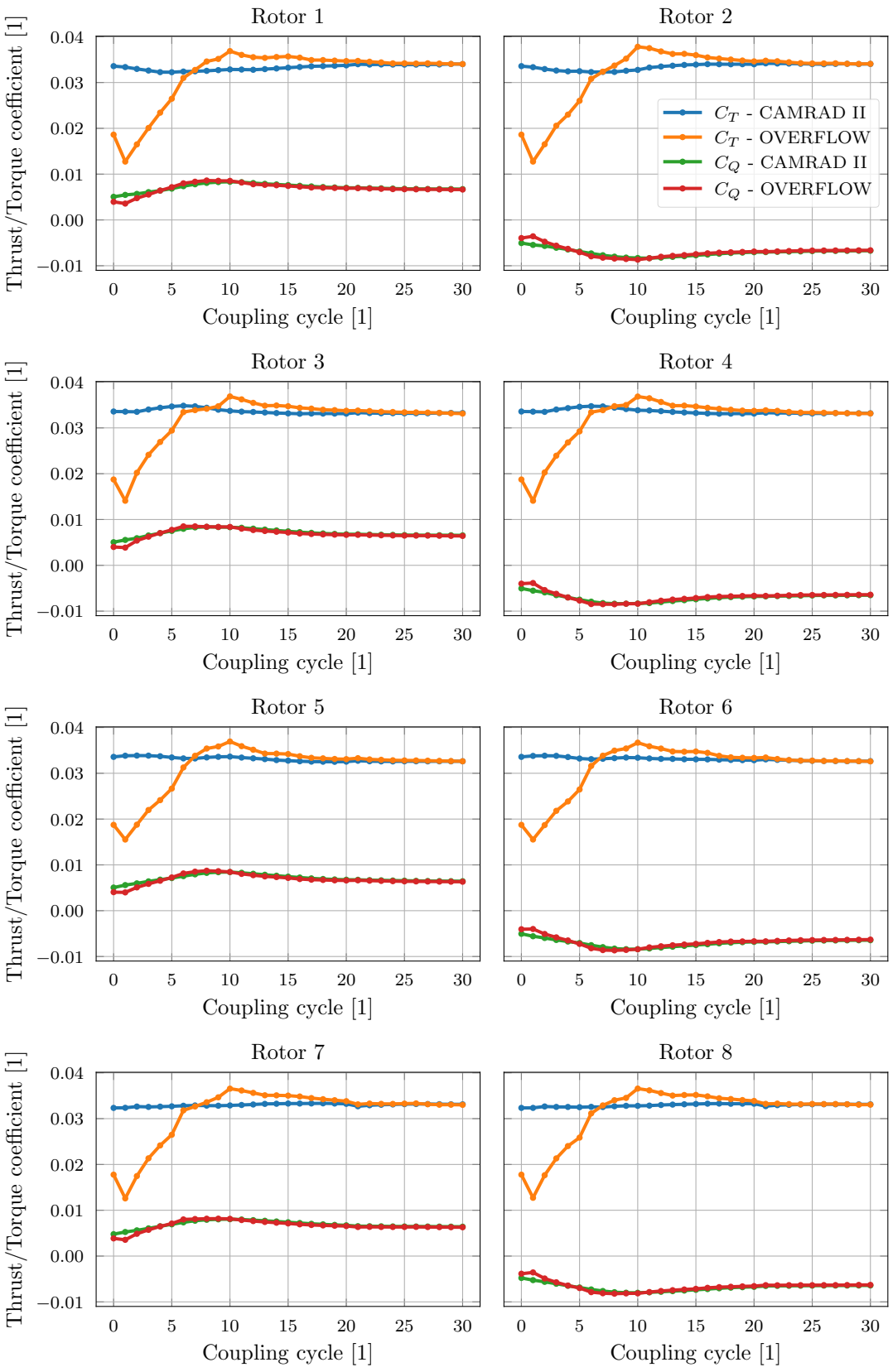

Fig. 14 Convergence history of thrust and torque coefficients in helicopter mode.

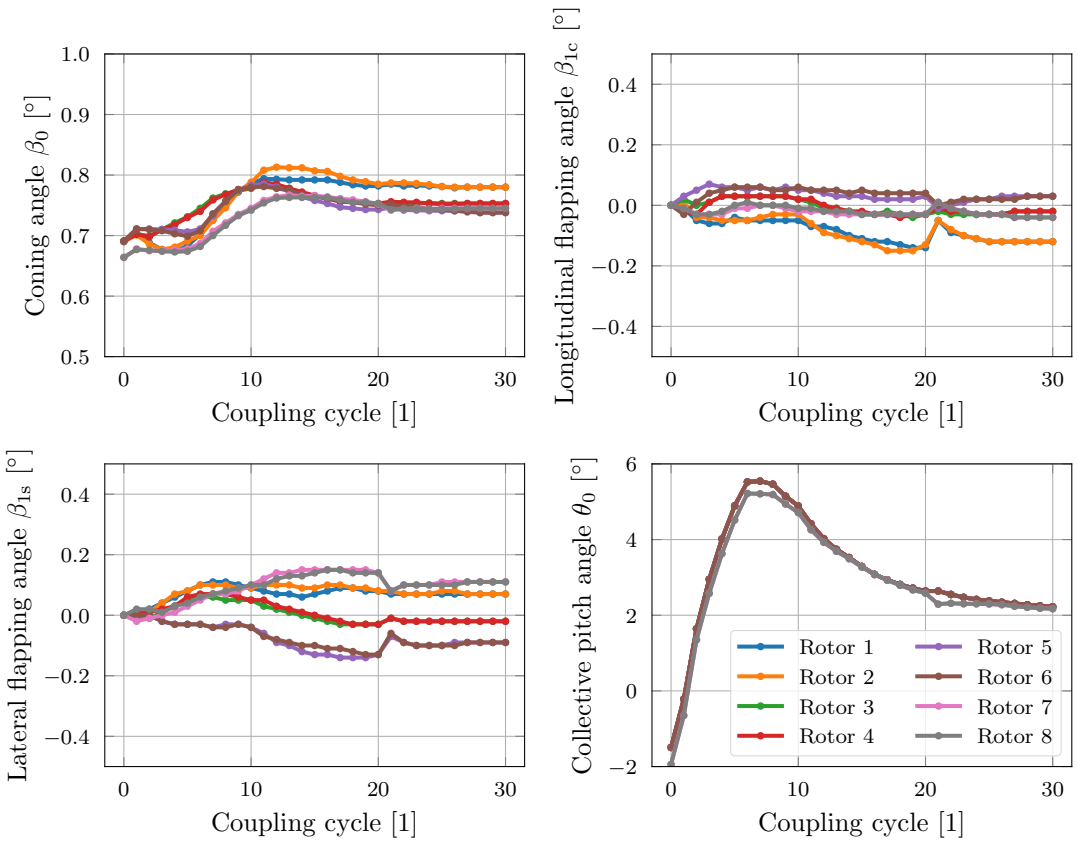

Fig. 15 Convergence history of the rotor trim angles in helicopter mode.

The aerodynamic loading is visualized through rotor maps of the normal force coefficient $M^2 c_n$ and chord force coefficient $M^2 c_c$ in Figs. 16 and 17. Disk planes are viewed from above and divided into four quadrants of 90°. The locations of the quadrants are reversed depending on the direction of rotation of the rotors.

Complex rotor-wake-airframe interactions cause an asymmetry of the aerodynamic loads. These changes are more noticeable for rotors closer to the fuselage (5–6 and 7–8) but less pronounced than those found in forward flight. Near the tip regions, one can observe peaks on the sectional normal and chord force corresponding to the blade-vortex interaction event occurring at the first blade passage. Near the root, no areas of negative lift are observed. On the one hand, the blades rotate at a higher rate than in airplane mode —see Table 1— and on the other hand, the axial flow through the rotor, due exclusively to the induced velocity, is lower than that of airplane mode. From equation 8, the inflow angle is significantly reduced and the angle of attack never becomes negative. This also explains why the trim values of the collective pitch in helicopter mode are much lower than those in airplane mode.

Finally, the contribution of each component to the force balance along the Z-axis is shown in Fig. 18. The mean vertical force F_z is time-averaged every 1440 steps, which corresponds to one rotor revolution. The equilibrium is established mainly between the gravity component due to the vehicle's weight and the thrust generated by the rotors. The percentage contribution is approximately 75-25 percent for the rotors located on the wing and tail, respectively. Although small in magnitude compared to the contribution of the rotors, the fuselage and the horizontal tail generate a downforce due to the induced velocity flow. Compared to airplane mode in Fig. 12, the aerodynamic forces acting on the fuselage took longer to converge. In fact, in order to stabilize them, the simulation was run for 10 extra revolutions after having achieved a converged solution for the rotors.

2. Wake geometry

Figure 19 shows oblique and top views of the vortex wake through the representation of iso-surfaces of Q-criterion colored by vorticity magnitude. The Q-criterion level was adjusted to a higher value than that of Fig. 13 to increase

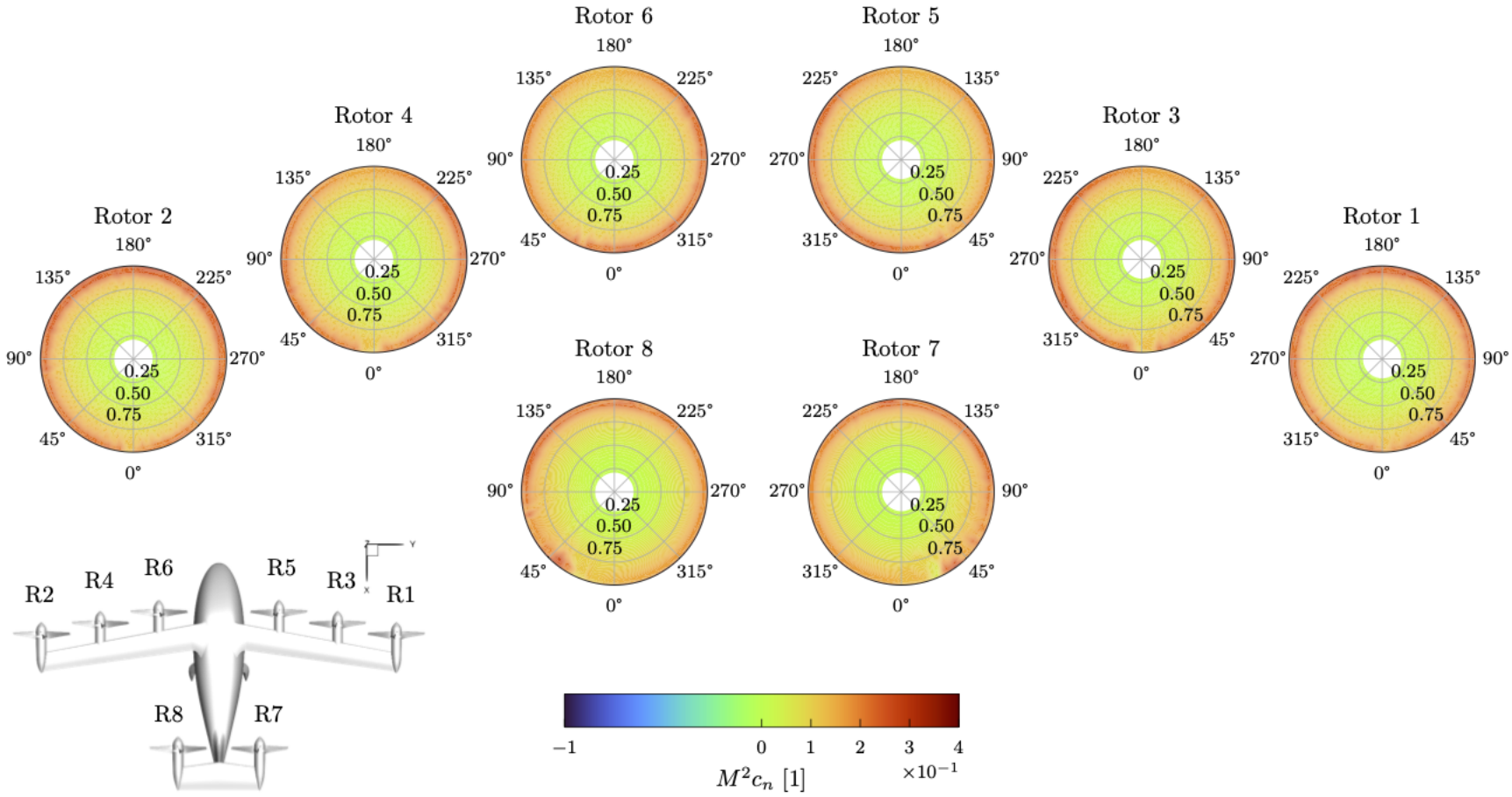

Fig. 16 Sectional normal force coefficient $M^2 c_n$ in hover.

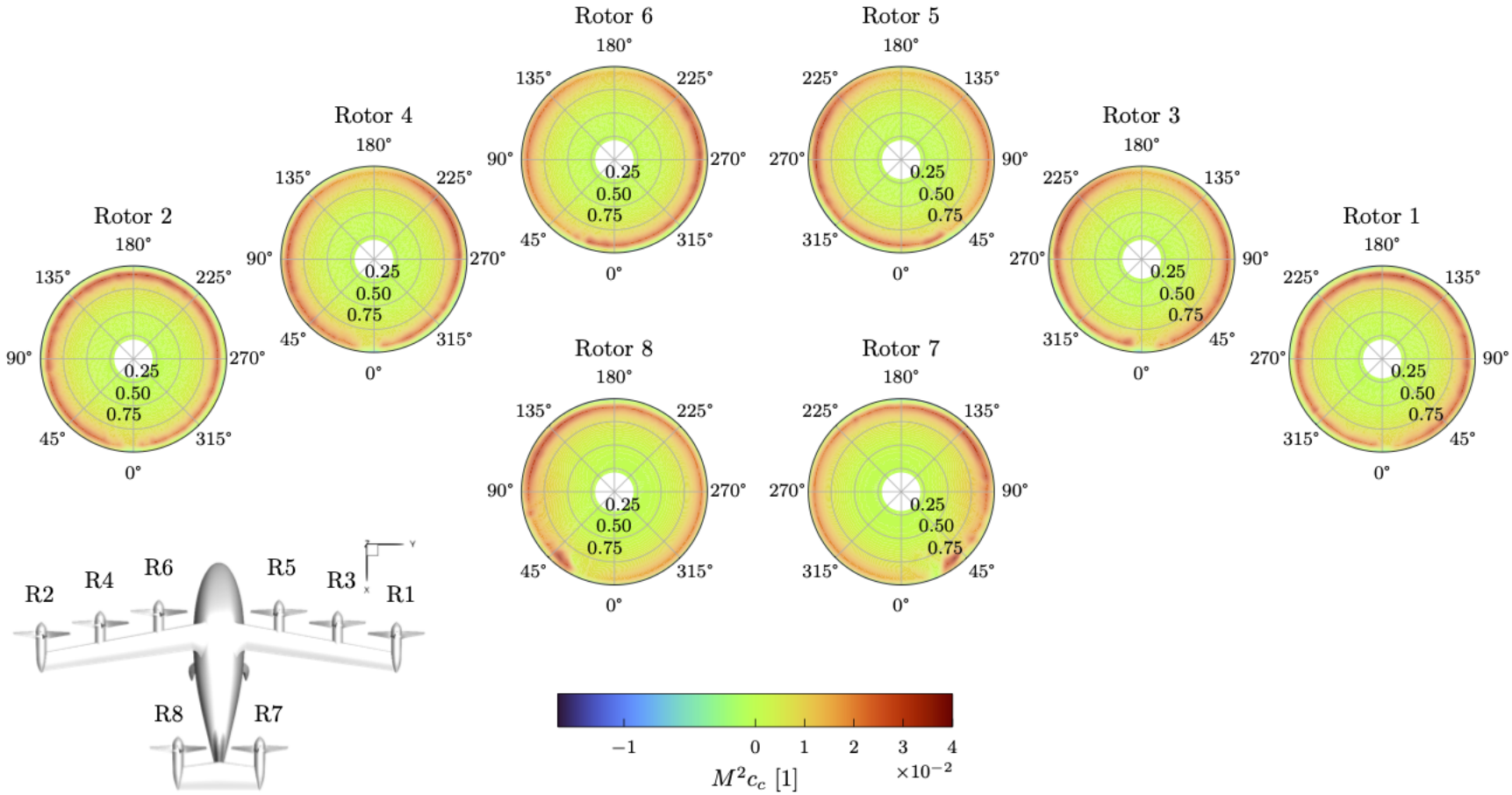

Fig. 17 Sectional chord force coefficient $M^2 c_c$ in hover.

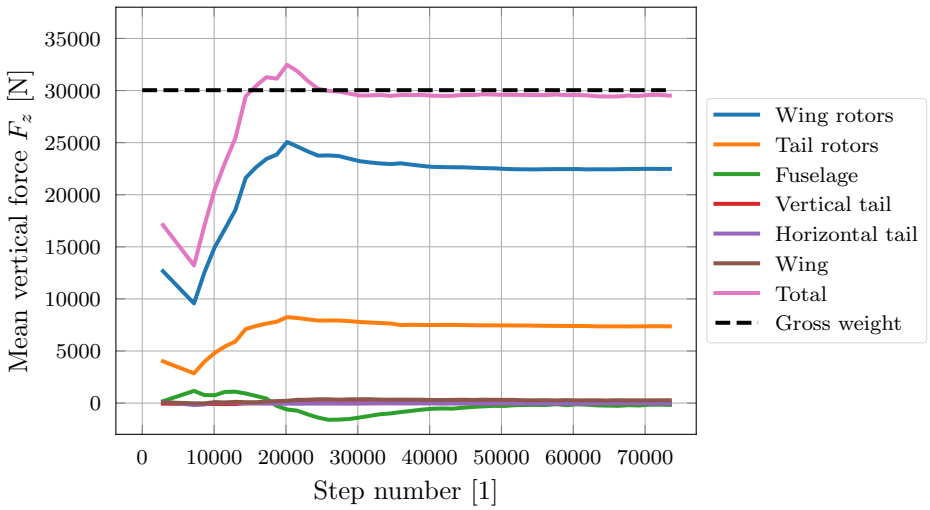

Fig. 18 Equilibrium of the mean vertical force as a function of the time step in helicopter mode.

the exposure of the fuselage while still portraying the main features of the wake. A well-defined tip-vortex structure emanates from the rotors tracing out helical trajectories as they are convected downwards. At a wake age of 360°, the vortices strike on the main wing or horizontal tail, then become unstable and disintegrate losing their structure. The descent rate is lower than that of airplane mode due to the lack of convective axial speed. Since the vortices remain appreciable time below the rotor, the blades are able to encounter the tip vortices shed by preceding blades, causing BVI events. Some vortical worm structures are visible around the tip vortices. Figure 19b shows the radial contraction of the wake.

3. Performance

To wrap up the analysis of helicopter mode, the performance of each individual rotor is measured in terms of the figure of merit (FM). This parameter is defined as the ratio of ideal rotor power to actual rotor power required for a given thrust:

$$\mathrm{FM} = \frac{T v_\mathrm{i}}{P}. \tag{10}$$

Note the similarities with equation 9 for the propulsive efficiency in airplane mode. Here the induced flow v_i replaces the freestream velocity V_∞.

Table 6 Rotor performance in helicopter mode measured by the figure of merit. The results are obtained from the coupled OVERFLOW/CAMRAD II approach and using CAMRAD II free wake analysis.

	Figure of merit FM	
	OVERFLOW/CAMRAD II	CAMRAD II free wake
Rotor 1	0.6593	0.7413
Rotor 2	0.6607	0.7413
Rotor 3	0.6554	0.7397
Rotor 4	0.6552	0.7397
Rotor 5	0.6474	0.7544
Rotor 6	0.6475	0.7544
Rotor 7	0.6653	0.7662
Rotor 8	0.6647	0.7662

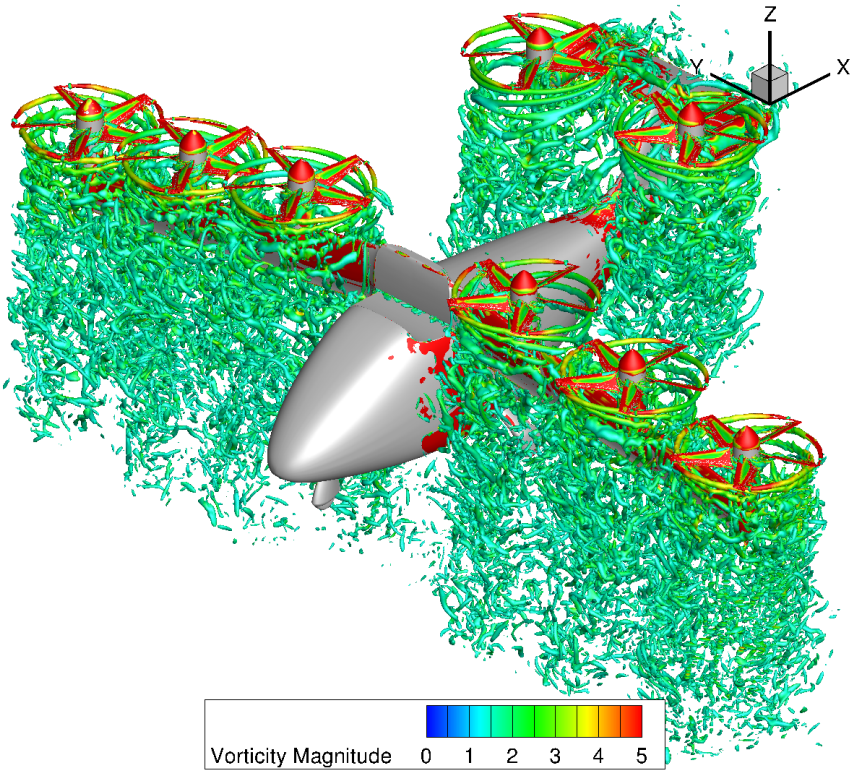

(a) Oblique view.

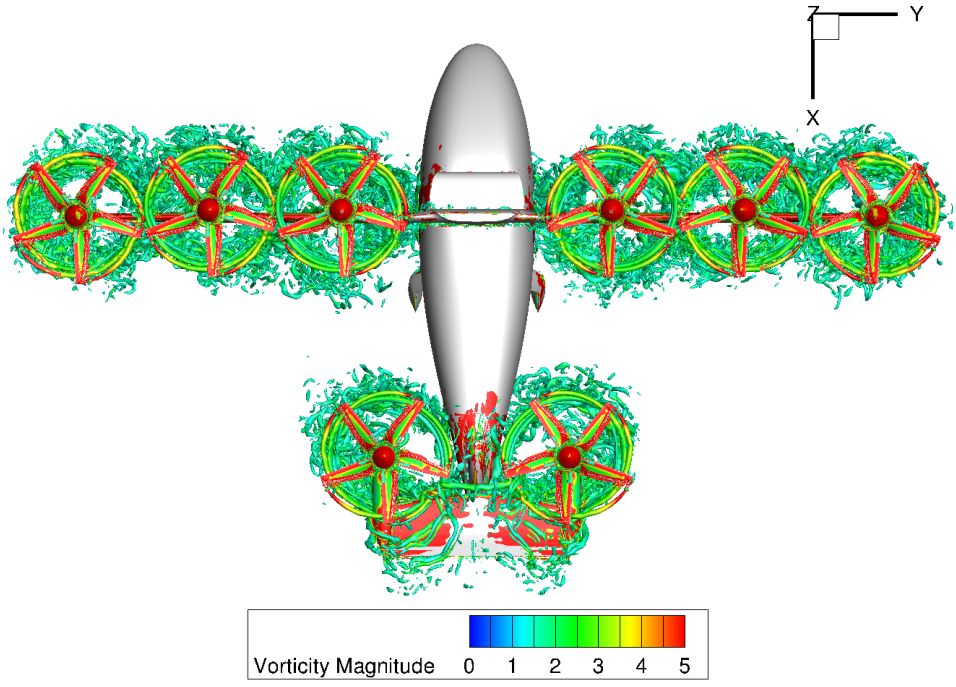

(b) Top view.

Fig. 19 Visualization of the wake geometry in helicopter mode through the representation of iso-surfaces of Q-criterion colored by vorticity magnitude.

Table 6 shows a comparison of the performances of each rotor, calculated by CAMRAD II using the CFD airloads and a free wake analysis. The latter overpredicts the FM by approximately 16 % when compared to the metrics obtained with the CFD aerodynamics. The differences are attributed to incomplete modeling of the interactional aerodynamics in the free wake approach. At the moment, there is no available wind tunnel data, but the results here obtained are left as a reference for future validation.

IV. Conclusion

NASA's tiltwing air taxi has been simulated in airplane and helicopter modes. A series of Tcl scripts have been written to automatize and parameterize the generation of overset surface and volume grids. High-fidelity CFD simulations using OVERFLOW were coupled with the comprehensive code CAMRAD II to solve the RANS equations in the resulting system of overset moving grids. With the loose copuling strategy, after each rotor revolution, the airloads from the CFD simulation are transferred to CAMRAD II, where the trim task finds the equilibrium solution for a steady-state operating condition, solving for performance, loads, and blade motions.

Simulations in airplane mode revealed complex rotor-wake-airframe interactions that affected sectional loads and rotor performance. For example, the main wing rotors operating close to the fuselage saw a 7.5 % decrease in propulsive efficiency compared to those located at the wing tips. The proximity to the fuselage introduces disturbances to the inflow of the propellers that add to the already high inflow angle. This effect reduces the angle of attack of the blade sections, creating large regions of negative thrust and drecreasing the net thrust production. Snapshots of the wake geometry showed a well-defined structure of tip vortices that rapidly convected downstream driven by the freestream velocity. This reduces the interaction with neighboring blades. Rotor-wake interactions were visualized as the wake of inboard rotors was pushed towards the fuselage and struck on the tail rotors. A breakdown of the vertical forces acting on the vehicle highlights the need of control surfaces as well as changes in attitude for proper trim.

In helicopter mode, there is a higher degree of symmetry in the sectional rotor airloads and no areas of negative lift were observed. The wake structure resembles the classical description of a rotor wake operating in hover, with tip vortices traveling downstream in contracting helical paths. BVI events occur after the first blade passage. The tip vortices become unstable after striking the wing and horizontal tail within a wake age of 360° and disintegrate. In this case, the trim of the vehicle was successfully controlled with the collective pitch angle of the rotors, as demonstrated by the equilibrium of vertical forces.

With the proliferation of new vehicle architectures as the UAM market expands, high-fidelity CFD has proven to be a mature tool to analyze these novel configurations. The comprehensive code CAMRAD II has also demonstrated its versatility to model unconventional vehicles, thanks to its flexible building-block approach. However, the performance metrics predicted by OVERFLOW and CAMRAD II free wake analysis differed as much as 10 % for inboard rotors in airplane mode, and 16 % for the same rotors in helicopter mode. Lower fidelity models need empirical corrections to model new configurations, and those could be provided by high-fidelity methods in conjunction with flight test data.

This initial study of NASA's tiltwing UAM concept sets up the steps for the numerical study of the transitional flight from helicopter to airplane mode, for which control surfaces will also be modeled.

Acknowledgments

This work is supported by the Revolutionary Vertical Lift Technology (RVLT) project (PM: Susan Gorton; TL: Brian Allan). The computations utilized the Pleiades, Electra, and Aitken supercomputers at the NASA Advanced Supercomputing Division. The authors would like to thank Wayne Johnson, Chris Silva, Gloria Yamauchi, and Brian Allan for helpful discussions.

References

[1] Nations, U., *The World's Cities in 2018*, United Nations, 2018. URL https://www.un-ilibrary.org/content/books/9789210476102.

[2] Yamauchi, G., "A Summary of NASA Rotary Wing Research: Circa 2008–2018," Tech. Rep. NASA/TP-2019-220459, NASA, December 2019.

[3] Johnson, W., and Silva, C., "NASA Concept Vehicles and the Engineering of Advanced Air Mobility Aircraft," *The Aeronautical Journal*, Vol. 126, No. 1295, 2022, pp. 59–91. https://doi.org/10.1017/aer.2021.92.

[4] Johnson, W., Silva, C., and Solis, E., "Concept Vehicles for VTOL Air Taxi Operations," *AHS Specialists Conference on Aeromechanics Design for Transformative Vertical Flight*, San Francisco, CA, 2018.

[5] Johnson, W., and Silva, C., "Observations from Exploration of VTOL Urban Air Mobility Designs," *Asian/Australian Rotorcraft Forum (ARF 2018)*, Jeju Island, Korea, 2018.

[6] Silva, C., and Johnson, W., "Practical Conceptual Design of Quieter Urban VTOL Aircraft," *VFS 77th Annual Forum*, Virtual Event, 2021.

[7] Patterson, M., Antcliff, K., and Kohlman, L., "A Proposed Approach to Studying Urban Air Mobility Missions Including an Initial Exploration of Mission Requirements," *AHS International 74th Annual Forum and Technology Display*, Phoenix, AZ, 2018.

[8] Whiteside, S., Pollard, B., Antcliff, K., Zawodny, N., Fei, X., Silva, C., and Medina, G., "Design of a Tiltwing Concept Vehicle for Urban Air Mobility," Tech. Rep. NASA/TM–20210017971, NASA, June 2021.

[9] Ventura Diaz, P., and Yoon, S., "High-Fidelity Computational Aerodynamics of the Elytron 4S UAV," *AHS Meeting*, San Francisco, CA, 2018.

[10] Ventura Diaz, P., Garcia Perez, D., and Yoon, S., "Computational Analysis of a Quiet Single-Main Rotor Helicopter for Air Taxi Operations," *VFS 78th Annual Forum*, Fort Worth, TX, 2022.

[11] Ventura Diaz, P., and Yoon, S., "Computational Study of NASA'S Quadrotor Urban Air Taxi Concept," *AIAA Paper 2020–0302*, 2020. https://doi.org/10.2514/6.2020-0302.

[12] Ventura Diaz, P., and Yoon, S., "High-Fidelity Simulations of a Quadrotor Vehicle for Urban Air Mobility," *AIAA Paper. 2022–0152*, 2022. https://doi.org/10.2514/6.2022-0152.

[13] Ventura Diaz, P., Johnson, W., Ahmad, J., and Yoon, S., "Computational Study of the Side-by-Side Urban Air Taxi Concept," *VFS 75th Annual Forum*, Philadelphia, PA, 2019, pp. 13–16.

[14] Ventura Diaz, P., and Yoon, S., "High-Fidelity Computational Aerodynamics of Multi-Rotor Unmanned Aerial Vehicles," *AIAA Paper 2018–1266*, 2018. https://doi.org/10.2514/6.2018-1266.

[15] Tran, S., Lim, J., Nunez, G., Wissink, A., and Bowen-Davies, G., "CFD Calculations of the XV-15 Tiltrotor During Transition," *VFS 75th Annual Forum*, Philadelphia, PA, 2019, pp. 13–16.

[16] Lim, J., "Fundamental Investigation of Proprotor and Wing Interactions in Tiltrotor Aircraft," *VFS 75th Annual Forum*, Philadelphia, PA, 2019, pp. 13–16.

[17] Pulliam, T., "High Order Accurate Finite-Difference Methods: as seen in OVERFLOW," *AIAA Paper 2011–3851*, 2011. https://doi.org/10.2514/6.2011-3851.

[18] Chan, W., Gomez, R., Rogers, S., and Buning, P., "Best Practices in Overset Grid Generation," *AIAA Paper 2002–3191*, 2002. https://doi.org/10.2514/6.2002-3191.

[19] Johnson, W., "Rotorcraft Aerodynamics Models for a Comprehensive Analysis," *American Helicopter Society 54th Annual Forum*, Vol. 54, Washington, D.C., 1998, pp. 71–94.

[20] Potsdam, M., Yeo, H., and Johnson, W., "Rotor Airloads Prediction Using Loose Aerodynamic/Structural Coupling," *Journal of Aircraft*, Vol. 43, No. 3, 2006, pp. 732–742. https://doi.org/10.2514/1.14006.

[21] Haimes, R., and Dannenhoffer, J., "The Engineering Sketch Pad: A Solid-Modeling, Feature-Based, Web-Enabled System for Building Parametric Geometry," *AIAA Paper 2013–3073*, 2013. https://doi.org/10.2514/6.2013-3073.

[22] Yoon, S., Chaderjian, N., Pulliam, T., and Holst, T., "Effect of Turbulence Modeling on Hovering Rotor Flows," *AIAA Paper 2015–2766*, 2015. https://doi.org/10.2514/6.2015-2766.

[23] Yoon, S., Lee, H., and Pulliam, T., "Computational Analysis of Multi-Rotor Flows," *AIAA Paper 2016—0812*, 2016. https://doi.org/10.2514/6.2016-0812.

[24] Yoon, S., Lee, H., and Pulliam, T., "Computational Study of Flow Interactions in Coaxial Rotors," *The AHS Technical Meeting on Aeromechanics Design for Vertical Lift*, San Francisco, CA, 2016.

[25] Spalart, P., "Comments on the Feasibility of LES for Wings, and on a Hybrid RANS/LES Approach," *The AFOSR International Conference on DNS/LES*, Greyden Press, 1997, pp. 137–147.

[26] Spalart, P., "Strategies for Turbulence Modelling and Simulations," *International Journal of Heat and Fluid Flow*, Vol. 21, No. 3, 2000, pp. 252–263.